HHS Public Access

Author manuscript

Math Models Methods Appl Sci. Author manuscript; available in PMC 2017 November 01.

Published in final edited form as:

Math Models Methods Appl Sci. 2016 November ; 26(12): 2341–2368. doi:10.1142/S021820251650055X.

Selection, calibration, and validation of models of tumor growth

E. A. B. F. Lima[*,¶], **J. T. Oden**[*,||], **D. A. Hormuth II**[*,**], **T. E. Yankeelov**[*,†,‡,††], and **R. C. Almeida**[§,‡‡]

[*]Center of Computational Oncology, Institute for Computational Engineering and Sciences, The University of Texas at Austin, 201 East 24th St, Austin, TX 78712-1229, USA

[†]Department of Internal Medicine, Livestrong Cancer Institutes, Dell Medical School, Health Learning Building, The University of Texas at Austin, 1501 Red River Street, Austin, TX 78712, USA

[‡]Department of Biomedical Engineering, The University of Texas at Austin, 107 W. Dean Keeton, Austin, TX 78712, USA

[§]National Laboratory for Scientific Computing (LNCC), Av. Getúlio Vargas, 333, Quitandinha, Petrópolis, Rio de Janeiro 25651-075, Brazil

Abstract

This paper presents general approaches for addressing some of the most important issues in predictive computational oncology concerned with developing classes of predictive models of tumor growth. First, the process of developing mathematical models of vascular tumors evolving in the complex, heterogeneous, macroenvironment of living tissue; second, the selection of the most plausible models among these classes, given relevant observational data; third, the statistical calibration and validation of models in these classes, and finally, the prediction of key Quantities of Interest (QOIs) relevant to patient survival and the effect of various therapies. The most challenging aspects of this endeavor is that all of these issues often involve confounding uncertainties: in observational data, in model parameters, in model selection, and in the features targeted in the prediction. Our approach can be referred to as "model agnostic" in that no single model is advocated; rather, a general approach that explores powerful mixture-theory representations of tissue behavior while accounting for a range of relevant biological factors is presented, which leads to many potentially predictive models. Then representative classes are identified which provide a starting point for the implementation of OPAL, the Occam Plausibility Algorithm (OPAL) which enables the modeler to select the most plausible models (for given data) and to determine if the model is a valid tool for predicting tumor growth and morphology (*in vivo*). All of these approaches account for uncertainties in the model, the observational data, the model parameters, and the target QOI. We demonstrate these processes by comparing a list of models for tumor growth, including reaction–diffusion models, phase-fields models, and models with and without mechanical deformation effects, for glioma growth measured in murine

[||]Corresponding author: oden@ices.utexas.edu.
[¶]lima@ices.utexas.edu
[**]david.hormuth@utexas.edu
[††]yankeelov@ices.utexas.edu
[‡‡]rcca@lncc.br

experiments. Examples are provided that exhibit quite acceptable predictions of tumor growth in laboratory animals while demonstrating successful implementations of OPAL.

Keywords

Predictive model; model calibration; computational oncology; cancer; systems biology

AMS Subject Classification

22E46; 53C35; 57S20

1. Introduction

The last decade has seen an explosion in literature on mathematical and computational models of the invasion and growth of tumors in living tissue. Examples include the recent survey paper,[27] books,[9,10] and the papers.[2,3] An elusive goal of studies in this broad area has been to create predictive models that capture the highly-complex array of biological, chemical, and physical events leading to the emergence and growth or decline of cancer in living organisms.[41,42]

The major challenges in tumor growth modeling remain the following: (1) *Model selection*. Among the enormous number of possible models covering a huge range of physical and biological events, which models are the "best" for predicting key Quantities of Interest (QOIs) in characterizing and measuring tumor growth? (2) *Model parameters*. How can we determine reasonable values or meaningful statistical representations of the multitude of parameters that appear in comprehensive models of tumor growth? (3) *Observational data*. How can one access observational data, both *in vitro* and *in vivo* data, to inform computational models and, at the same time, cope with experimental noise and inevitable errors in the processes and systems used to collect and process data? (4) *Algorithms*. What new computational algorithms are needed to cope with stochastic systems, highly-complex geometries, very large statistical sampling problems, numerical stability, very large scalable parallel computing requirements, error estimation and control, adaptive meshing, statistical inversions, image segmentation, classification and registration, and other computational issues? (5) *Results and actions*. How is the validity of the model predictions assessed; how is the uncertainty in the predicted QOIs quantified; and how can the model predictions guide effective therapies for controlling or eliminating tumor growth?

While some progress has been made in recent years in all of these grand-challenge areas, many open problems remain, and the development of approaches to tumor growth modeling remains a subject of active research. In Refs. 15 and 26 general phenomenological models of growth of tumors in living tissue are proposed and a Bayesian setting is presented as a basis for statistical calibration and validation of tumor models. The notion of Bayesian model plausibilities, mentioned in the classical work of Jeffreys,[18] was introduced in Ref. 28 as a rigorous approach to the selection of tumor growth models. A general class of multi-species tissue models of tumor growth is presented in Ref. 24 and algorithms for assessing the sensitivities of model parameters and for solving stochastic systems describing such models

is given in Ref. 23. The Occam Plausibility Algorithm (OPAL) has been proposed as an adaptive process for model selection and validation in the presence of uncertainties, [12,25] and has been applied to the classical problem of generating coarse-grained molecular models for large atomistic systems. Its application to the selection of tumor models is taken up for the first time in the present study.

In this work, we develop a general framework for constructing models of tumor growth that begins with the construction of classes of phenomenological models of tissue behavior. For observational data, we draw from work on glioma rat models described in Ref. 17.

In Sec. 2, we describe a general approach for developing a large class of models that employs a combination of continuum mixture theory to handle large numbers of interacting species, the balance laws of continuum physics, and the principal hallmarks of cancer advocated in Refs. 13 and 14. From this we lay down a large family of models that include the phase-field models of Ref. 24, the reaction–diffusion models of Refs. 38 and 39, and the effects of mechanical deformation of tumors and the extracellular matrix.

2. Construction of Mathematical Models of Tumor Growth

The major challenges in developing phenomenological models of tumor growth are: (1) to cope with the highly heterogeneous system of interacting constituents in the complex environment encountered in living tissue (viable tumor cells, hypoxic cells, extracellular matrix, nutrients, etc.); (2) to develop mathematical relations that are consistent with (and do not violate) basic physical laws; and (3) to incorporate mathematical characterizations of biological phenomena generally accepted to be responsible for the emergence, growth, or decline of cancer in living organisms. To address (1), we appeal to mixture theory, in which an interacting mass of species is represented by N scalar fields representing the volume fractions or mass concentrations of each constituent. To address (2), we again call upon the very successful theory of continuum mechanics of mixtures, and to address (3) we attempt to develop mathematical characterizations of hypotheses suggested by the well-known eight Hallmarks of Cancer of Hanahan and Weinberg.[14] We provide brief reviews of these fundamental components in the subsections that follow. As will become evident, this model-building strategy leads to a very large class of possible models of tumor growth. Which models are valid among these is a central question in predictive science and a subject taken up in Secs. 3 and 4.

2.1. Continuum mixture theory

The fundamental idea underlying continuum mixture theory, developed in the early papers of Truesdell,[35] Truesdell and Toupin,[36] Eringen and Ingram[11] and described in the comprehensive memoir of Bowen[4] and the monograph of Rajagopal and Tao,[31] is that a material body $\mathcal{B}$ can be considered to be composed of N constituent species $\mathcal{B}_1, \mathcal{B}_2, \ldots, \mathcal{B}_N$ that occupy a common portion Ω of physical space at the same time. Each constituent is assigned a mass density $\hat{\rho}_\alpha$, representing the mass of the αth constituent per unit volume, considered as a function of the spatial position $\mathbf{x}$ of material points of $\mathcal{B}$ and of time t. The mass density of the mixture is then $\rho = \rho(\mathbf{x}, t) = \sum_{\alpha=1}^{N} \hat{\rho}_\alpha(\mathbf{x}, t)$ and the mass concentration of

the αth constituent is defined by $c_\alpha = \hat{\rho}_\alpha/\rho$. If dv_α is a differential volume element occupied by constituent α and dv is a volume element containing point $(\mathbf{x}, t)$, then $\phi_\alpha(\mathbf{x}, t) = dv_\alpha/dv$ is the volume fraction of the αth constituent at the point. We have the relations, $\rho c_\alpha = \rho_\alpha \phi_\alpha = \hat{\rho}_\alpha$, and

$$\sum_{\alpha=1}^{N} c_\alpha(\mathbf{x}, t) = 1 \quad \text{and} \quad \sum_{\alpha=1}^{N} \phi_\alpha(\mathbf{x}, t) = 1. \tag{2.1}$$

Thus, the major feature of a continuum mixture theory is that one can distinguish one species from another at a point $(\mathbf{x}, t)$ in a body at time t by simply specifying its volume fraction $\phi_\alpha(\mathbf{x}, t)$ (or its mass concentration $c_\alpha(\mathbf{x}, t)$), thereby avoiding the need to impose interface conditions between different species, all subject to conditions (2.1). The influence of one species on another is manifested through flux and source contributions that enter through imposing conservation (balance) laws drawn from continuum physics. Confining ourselves to mechanical phenomena by ignoring thermal effects, these laws at the constituent level take on the following forms:

Conservation of mass:

$$\frac{\partial}{\partial t}(\rho_\alpha \phi_\alpha) + \nabla \cdot (\rho_\alpha \phi_\alpha \mathbf{v}_\alpha) = \rho_\alpha (S_\alpha - \nabla \cdot \mathbf{J}_\alpha); \tag{2.2}$$

Conservation (*balance*) *of linear momentum*:

$$\rho_\alpha \phi_\alpha \frac{\partial \mathbf{v}_\alpha}{\partial t} = \nabla \cdot \mathbf{T}_\alpha + \rho_\alpha \phi_\alpha \mathbf{b}_\alpha + \hat{\mathbf{p}}_\alpha; \tag{2.3}$$

Conservation (*balance*) *of angular momentum*:

$$\mathbf{T}_\alpha - \mathbf{T}_\alpha^T = \mathbf{m}_\alpha; \tag{2.4}$$

Conservation of energy:

$$\rho_\alpha \phi_\alpha \frac{\partial e_\alpha}{\partial t} = \operatorname{tr} \mathbf{T}_\alpha \mathbf{L}_\alpha + \hat{\varepsilon}_\alpha + \Upsilon_\alpha; \tag{2.5}$$

The second law of thermodynamics (*the Clausius–Duhem inequality*):

$$\sum_{\alpha=1}^{N} \left\{ \rho_\alpha \phi_\alpha \frac{d^\alpha \eta_\alpha}{dt} + \Gamma_\alpha \eta_\alpha + \nabla \cdot (\mathbf{H}_\alpha - \rho_\alpha \phi_\alpha \eta_\alpha \mathbf{u}_\alpha) \right\} \geq 0. \tag{2.6}$$

Here $d^{\alpha}/dt = d/dt + \mathbf{v}_{\alpha} \cdot \nabla$, ∇ being the spatial gradient operator and $\mathbf{u}_{\alpha} = \mathbf{v}_{\alpha} - \mathbf{v}$. The definition of terms used in these relations is presented in Table 1. Full details on this theory and the role of constraints on the species balance laws imposed by the entropy inequality and the sums of the constituent laws that must be consistent with the full-mixture balance laws for the continuum are laid out in Ref. 26.

Our next step is to reduce the complexity of this system through the use of common simplifying assumptions: we shall assume that $\rho_{\alpha} = \rho_0 =$ constant for all species, neglect inertial effects, set $\mathbf{m}_{\alpha} = \mathbf{0}$ (i.e. a mono-polar material), $\mathbf{b}_{\alpha} = \mathbf{0}$, ignore temperature and thermal effects, and treat the tumor as a solid mass of tumor cells; they are all higher-order effects and need not be considered in this first contribution. Following Ref. 26, the constitutive law for mass flux entering constituent α is

$$\mathbf{J}_{\alpha} = -\sum_{\beta=1}^{N} M_{\alpha\beta}(\boldsymbol{\phi}) \nabla \mu_{\alpha\beta}, \tag{2.7}$$

where $M_{\alpha\beta}(\boldsymbol{\phi})$ is the positive-semidefinite mobility matrix which may depend upon the volume fractions $\boldsymbol{\phi} = (\phi_1, \phi_2, \ldots, \phi_N)$ and $\mu_{\alpha\beta}$ is the chemical potential. This particular law for mass flux manifests itself naturally from the second law of thermodynamics as the singular law, linear in the chemical potential, that is consistent with the Clausius–Duhem inequality (see Ref. 26). As shown in Ref. 26, if the Helmholtz free energy per unit volume Ψ_{α} is a function of species volume fractions and their spatial gradients, then $\mu_{\alpha\beta}$ can be derived from Ψ_{α} according to

$$\mu_{\alpha\beta} = \frac{\partial \Psi_{\alpha}}{\partial \phi_{\beta}} - \nabla \cdot \frac{\partial \Psi_{\alpha}}{\partial \nabla \phi_{\beta}}. \tag{2.8}$$

With these assumptions and (2.7) and (2.8) enforced, the evolution of various species described by (2.2) is now governed by the equation

$$\frac{\partial \phi_{\alpha}}{\partial t} = \nabla \cdot \sum_{\beta=1}^{N} M_{\alpha\beta}(\boldsymbol{\phi}) \nabla \left(\frac{\partial \Psi_{\alpha}}{\partial \phi_{\beta}} - \nabla \cdot \frac{\partial \Psi_{\alpha}}{\partial \nabla \phi_{\beta}} \right) + S_{\alpha}(\boldsymbol{\phi}). \tag{2.9}$$

The source terms $S_{\alpha}(\boldsymbol{\phi})$ must reflect the interactions taking place among constituents that encompass biological events leading to proliferation, hypoxic and necrotic differentiation of cancer cells, nutrient transport, etc.

Likewise, a possible constitutive equation for the partial stress $\mathbf{T}_{\alpha}$ with hyperelastic deformable constituents is given by

$$\mathbf{T}_\alpha = \left(\Psi_\alpha - \sum_{\beta=1}^{N} \mu_{\alpha\beta}\phi_\alpha\right)\mathbf{I} - \sum_{\beta=1}^{N} \frac{\partial \psi_\alpha}{\partial \nabla \phi_\beta} \otimes \nabla\phi_\beta + \det\mathbf{F}_\alpha \mathbf{F}_\alpha \left(2\frac{\partial W_\alpha}{\partial \mathbf{C}_\alpha}\right)\mathbf{F}_\alpha^{-T}, \tag{2.10}$$

where $\mathbf{F}_a$ is the deformation gradient, W_a is the stored energy, and $\mathbf{C}_\alpha = \mathbf{F}_\alpha^{-T}\mathbf{F}_\alpha$ is the right Cauchy–Green tensor for the ath constituent. Clearly, the mechanical behavior of the mixture can be characterized by free energy functions Ψ_a which are functions of volume fractions, their gradients, and some deformation measure such as $\mathbf{C}_a$.

2.2. The hallmarks of cancer

The remaining steps in developing predictive models of tumor growth must attempt to capture a multitude of complex biological events present in the differentiation of cancer cells in living tissue. In a famous pair of papers, Hanahan and Weinberg[13,14] proposed eight Hallmarks of Cancer as traits shared by the majority of cancer types. These are depicted in Fig. 1. The source terms S_a in (2.9) must be designed to model these traits in some fashion.

As an example, consider a 12-species model in which the volume fraction of cell types are:

- $\phi_1 = \phi_T$ = Tumor cells;
- $\phi_2 = \phi_H$ = Hypoxic cells;
- $\phi_3 = \phi_N$ = Necrotic cells;
- $\phi_4 = \phi_C$ = Healthy cells;
- $\phi_5 = \phi_\sigma$ = Nutrient-rich extracellular water (e.g. glucose);
- $\phi_6 = \phi_{\sigma_o}$ = Nutrient-poor extracellular water;
- $\phi_7 = \phi_{\text{TAF}}$ = Tumor Angiogenesis Factor (TAF) rich extracellular water (promoting vascular sprouting to supply nutrients to cancer cells);
- $\phi_8 = \phi_{\text{TAF}_o}$ = TAF-poor extracellular water;
- $\phi_9 = \phi_e$ = Proliferative endothelial cells;
- $\phi_{10} = \phi_{e_o}$ = Non-activated endothelial cells;
- $\phi_{11} = \phi_{\text{MDE}}$ = Matrix Degrading Enzyme (MDE) rich extracellular water;
- $\phi_{12} = \phi_{\text{MDE}_o}$ = MDE-poor extracellular water.

We also model an unknown displacement field, $\mathbf{u} = \mathbf{u}(\mathbf{x}, t)$, to depict motions (and deformations) and measure mechanical effects present in the tissue domain. The extracellular matrix ($\phi_{13} = \phi_{\text{ECM}}$), the surrounding material that lies between cells and plays important role on the pattern of new blood vessels, is assumed to be non-motile and is degraded by soluble MDE and remodeled by the tumor cells (see Ref. 27). Following Ref. 24, we only need to model the complementary species, e.g. $\phi_C = 1 - \phi_T$. Examples of source terms designed to depict biological events laid out in Fig. 1 are:

$$
\begin{aligned}
S_T &= \lambda_T^{\text{prol}}\phi_\sigma(\phi_T-\phi_H-\phi_N)-\lambda_T^{\text{apop}}(\phi_T-\phi_N);\\
S_H &= -\lambda_H^{\text{apop}}\phi_H+\lambda_{PH}\mathcal{H}(\sigma_{PH}-\phi_\sigma)\phi_P-\lambda_{HP}\mathcal{H}(\phi_\sigma-\sigma_{HP})\phi_H-\lambda_{HN}\mathcal{H}(\sigma_{HN}-\phi_\sigma)\phi_H;\\
S_N &= \lambda_{HN}\mathcal{H}(\sigma_{HN}-\phi_\sigma)\phi_H;\\
S_\sigma &= -\lambda_T^{\text{prol}}\phi_\sigma(\phi_T-\phi_H-\phi_N)-\lambda_H^{\text{cons}}\phi_\sigma\phi_H+\lambda_T^{\text{apop}}(\phi_T-\phi_N)+\alpha_R(1-\phi_\sigma)\phi_e;\\
S_{\text{TAF}} &= +\lambda_{\text{TAF}}(1-\phi_{\text{TAF}})\phi_H-\alpha_{\text{TAF}}\phi_{\text{TAF}}\phi_e\mathcal{H}(\phi_{\text{TAF}}-\phi_{\text{TAF}_c});\\
S_e &= \alpha_P(\phi_{\text{TAF}})\phi_e\mathcal{H}(\phi_{\text{TAF}}-\phi_{\text{TAF}_c});\\
S_{\text{MDE}} &= \lambda_{\text{prod}}^{\text{MDE}}(1-\phi_{\text{MDE}})(\phi_T-\phi_N)-\lambda_{\text{decay}}^{\text{MDE}}\phi_{\text{MDE}}-\lambda_{\text{decay}}^{\text{ECM}}\phi_{\text{ECM}}\phi_{\text{MDE}};\\
S_{\text{ECM}} &= -\lambda_{\text{decay}}^{\text{ECM}}\phi_{\text{ECM}}\phi_{\text{MDE}}+\lambda_{\text{rem}}^{\text{ECM}}(\phi_T-\phi_N)(1-\phi_{\text{ECM}}),
\end{aligned}
\tag{2.11}
$$

where $\mathcal{H}(\phi)$ is the Heaviside function whose value is one if ϕ is positive and zero otherwise. In (2.11), the tumor cells can grow when the proliferative tumor cells ($\phi_P = \phi_T - \phi_H - \phi_N$) uptake nutrients in order to enter mitosis (divide) and decrease due to the apoptosis of the viable cells ($\phi_V = \phi_P + \phi_H$). The hypoxic cells can die or change to other phenotypic states depending on the nutrient threshold. If $\phi_\sigma < \sigma_{PH}$, the proliferative cells become hypoxic; however, if the nutrient volume fraction increases, so $\phi_\sigma > \sigma_{HP}$, the hypoxic cells return to the proliferative phenotype, and if $\phi_\sigma < \sigma_{HN}$, the hypoxic cells change to the necrotic state. The nutrient volume fraction can increase due to the growth of new blood vessels. The hypoxic cells release TAF that promotes the endothelial cells to proliferate and migrate up the TAF concentration gradient toward the source. The MDE are produced by the viable tumor cells and has a natural decay. The extracellular matrix is remodeled by the viable tumor cells and degraded by the MDE. In order to capture the angiogenesis process, we integrate to the continuum tissue-scale model an Agent-Based Model (ABM) that guides the movement of the endothelial tip cell.[23] Results for subclasses of this model can be seen in Refs. 24 and 23.

3. Classes of Parametric Models of Tumor Growth

The fundamental idea of a mathematical model of a natural event is that a model embodies a mathematical abstraction based of inductive and testable hypotheses laid down in an attempt to explain observed phenomena. Models are surrogates of scientific theory and, thus, are representatives of a fundamental pillar of science designed to acquire knowledge about the causes and effects of physical and biological phenomena and to predict events that occur under known or assumed conditions. We subscribe to the philosophy of Box[5] who observed that “all models are wrong, but some can be useful”. Our goal is not only to develop useful models but also methods to estimate exactly how useful models are in predicting of realistic phenomena prevalent in tumor emergence and growth.

As a first step, we develop a set of model classes of macroscale (tissue-level) models $\mathfrak{M}$ of the form

$$\mathscr{M}=\{\mathscr{P}_1(\boldsymbol{\theta}_1),\mathscr{P}_2(\boldsymbol{\theta}_2),\ldots,\mathscr{P}_m(\boldsymbol{\theta}_m)\}, \quad (3.1)$$

where $\mathscr{P}_i(\boldsymbol{\theta}_i)$ is a class of models parametrized by parameters $\boldsymbol{\theta}_i$ which belong to a parameter space $\Theta_i \subset \mathbb{R}^{d_i}$, $d_i < \infty$. Each model class is a mathematical model, symbolically written as

$$\mathscr{P}_i \sim A_i(\boldsymbol{\theta}_i, S; u_i(S, \boldsymbol{\theta}_i)) = 0, \quad (3.2)$$

where $A_i(\cdot)$ is a collection of mathematical operators, S is the scenario in which the model is implemented and $u_i(S, \boldsymbol{\theta}_i)$ is the solution to the forward problem. The notion of a model scenario is important in the science of model selection and validation: the term scenario is used to describe the parameter-independent domain in which the problem (3.2) is posed and, interchangeably, the physical environment in which observational data are collected to calibrate or validate the model, or to solve the forward problem in the full prediction scenario S_P. Examples are the collection of *in vitro* data for a calibration scenario S_C, collection of *in vivo* data for validation scenarios S_V, and the full-model prediction in a scenario S_P. Other examples involve cross-validation processes in which a model is "trained" in a calibration scenario and then validated or rejected in the validation scenario. The application discussed in Sec. 6 involves such scenarios.

3.1. Bayesian model calibration and validation

The use of a Bayesian framework for statistical model calibration and validation in the presence of uncertainties is discussed in detail in Refs. 12 and 25. The basic ideas involve the following steps:

1. Beginning with one or more calibration scenarios, S_C, in which observational data, $\mathbf{y}_C$, are collected and given a prior probability density, $\pi^C_{\text{prior}}(\boldsymbol{\theta})$, on the vector of model parameters $\boldsymbol{\theta} \in \Theta$, compute the posterior probability density π^C_{post} from the relation

$$\pi^C_{\text{post}}(\boldsymbol{\theta}|\mathbf{y}_C) = \frac{\pi^C_{\text{like}}(\mathbf{y}_C|\boldsymbol{\theta})\pi^C_{\text{prior}}(\boldsymbol{\theta})}{\pi^C_{\text{evid}}(\mathbf{y}_C)}; \quad (3.3)$$

where $\pi^C_{\text{like}}(\mathbf{y}_C|\boldsymbol{\theta})$ is the calibration likelihood function and $\pi^C_{\text{evid}}(\mathbf{y}_C) = \int_\Theta \pi^C_{\text{like}}(\mathbf{y}_C|\boldsymbol{\theta})\pi^C_{\text{prior}}(\boldsymbol{\theta})d\boldsymbol{\theta}$ is the model evidence.

2. Using $\pi^C_{\text{post}}(\boldsymbol{\theta}|\mathbf{y}_C)$ as a prior update, the parameters in validation tests in validation scenario S_V, with observational data $\mathbf{y}_V$, using the relation

$$\pi^V_{\text{post}}(\boldsymbol{\theta}|\mathbf{y}_V,\mathbf{y}_C)=\frac{\pi^V_{\text{like}}(\mathbf{y}_V|\boldsymbol{\theta})\pi^C_{\text{post}}(\boldsymbol{\theta}|\mathbf{y}_C)}{\pi^V_{\text{evid}}(\mathbf{y}_V,\mathbf{y}_C)}, \quad (3.4)$$

with $\pi^V_{\text{post}}(\cdot|\cdot)$, $\pi^V_{\text{like}}(\cdot|\cdot)$, and $\pi^V_{\text{evid}}(\cdot|\cdot)$ the validation posterior, likelihood and evidence Probability Density Functions (PDFs), respectively.

3. Using the updated parameters $\boldsymbol{\theta}$ computed in (3.4), solve the forward problem in the final validation scenario S_V for the model approximation $\mathbf{d}_V(\boldsymbol{\theta})$ of $\mathbf{y}_V$, and determine if the prediction accuracy meets a preset tolerance γ_{tol}, e.g.

$$\|\mathbf{d}_V(\boldsymbol{\theta})-\mathbf{y}_V\| \leq \gamma_{\text{tol}}, \quad (3.5)$$

$\|\cdot\|$ being an appropriate norm. If this tolerance is met, the model is declared *not invalid*. Otherwise, the model is invalid and the model is rejected.

4. If the model is declared not invalid, use the validation parameter $\boldsymbol{\theta}$ in the full prediction scenario S_P to solve the forward problem $A(\boldsymbol{\theta}, S_P, u(S_P, \boldsymbol{\theta})) = 0$ and use the solution to compute the QOI $Q(u(S_P, \boldsymbol{\theta}))$.

The statistical inverse problems (3.3) and (3.4) are solved using appropriate sampling algorithms such as Markov-Chain Monte Carlo (MCMC). The forward problem in Step (4) is solved using any appropriate stochastic solver employing, for example, the Monte Carlo method, stochastic collocation, etc. (see e.g. Refs. 22, 29 and 23). The norm in (3.5) symbolizes any of several measures of distance between the PDFs $\mathbf{d}_V(\boldsymbol{\theta})$ and $\mathbf{y}_V$. We frequently employ the Kullback–Leibler divergence $D_{\text{KL}}(\cdot\|\cdot)$, which measures the difference in information content between probability distributions: for PDFs $\mathbf{q}$ (data) and $\mathbf{p}$ (prediction),

$$D_{\text{KL}}(\mathbf{q}\|\mathbf{p})=\int_{\mathscr{Y}}\mathbf{q}(\mathbf{y})\log\frac{\mathbf{q}(\mathbf{y})}{\mathbf{p}(\mathbf{y})}d\mathbf{y}, \quad (3.6)$$

$\mathscr{Y}$ being the space in which observational data are sampled. The choice of a suitable metric is often a subjective one. The $D_{\text{KL}}(\cdot\|\cdot)$ is a natural measure of relative information entropy between two PDFs. We may also add weights, such as the variance σ^2 in data, yielding measures "$D_{\text{KL}}(\sigma^2)$". We employ such measures in the applications discussed in Sec. 7.

3.2. Model sensitivities

Given a parametric model $\mathscr{P}$, with a parameter set $\boldsymbol{\theta}$, the fundamental issue of parameter sensitivity naturally arises: to what extent do variations in model parameters affect the target QOIs? This question can be addressed by computing model sensitivities — a topic addressed extensively in the literature; see, for example, the books of Saltelli.[32,33]

The general approach is to pick an output function $Y(\boldsymbol{\theta})$ that depends upon the parameters $\boldsymbol{\theta}$ ($Y(\boldsymbol{\theta})$ can, in some cases, be taken to be the QOI, $Q(\boldsymbol{\theta})$) and to compute changes in $Y(\boldsymbol{\theta})$ due to small perturbations (δ) in each parameter, taken one at a time, the other parameters being held constant. In this way, parameter sensitivity indexes can be computed to assess the relative influence of model parameters on $Y(\boldsymbol{\theta})$.

An example of such sensitivity measures is the elementary effects method (see Refs. 32 and 33):

$$EE_i = \frac{[y(\theta_1, \theta_2, \ldots, \theta_{i-1}, \theta_i + \delta, \theta_{i+1}, \ldots, \theta_k) - y(\theta_1, \theta_2, \ldots, \theta_k)]}{\delta}.$$

The total sensitivity of the parameter is given by

$$\mu_i^* = \frac{1}{N_t} \sum_{j=1}^{N_t} |EE_i^j|, \tag{3.7}$$

where N_t is the number of trajectories. If a parameter is judged to have little impact on the outcome $Y(\boldsymbol{\theta})$, then the model featuring this parameter can be discarded, often resulting in a great simplification of the model to be used in the prediction of the QOI. Examples of model sensitivity calculations for tumor models can be found in Ref. 23.

3.3. Model plausibility

A fundamental question of overriding importance in modeling tumor growth (and, indeed, in all of predictive science) is that of selecting the mathematical model most appropriate for the predicting QOIs. A general approach to model selection is embodied in the notion of model plausibility, attributed originally to Jeffreys[18] and later proposed by Chow,[7] Beck,[1] Prudencio and Cheung,[29] and Oden *et al.*[25] The basic idea is this: given observational data $\mathbf{y}$ and a set of m models $\mathscr{M} = \{\mathscr{P}_j(\boldsymbol{\theta}_j)\}_{j=1}^m$, each model $\mathscr{P}_j$ having its own parameters $\boldsymbol{\theta}_j \in \Theta_j$, rewrite Bayes' rule acknowledging that probabilities are conditional on the model $\mathscr{P}_j$ and the set $\mathscr{M}$:

$$\pi_{\text{post}}(\boldsymbol{\theta}_j | \mathbf{y}, \mathscr{P}_j, \mathscr{M}) = \frac{\pi_{\text{like}}(\mathbf{y} | \boldsymbol{\theta}_j, \mathscr{P}_j, \mathscr{M}) \pi_{\text{prior}}(\boldsymbol{\theta}_j | \mathscr{P}_j, \mathscr{M})}{\pi_{\text{evid}}(\mathbf{y}|, \mathscr{P}_j, \mathscr{M})}. \tag{3.8}$$

The model evidence is the marginalization of the numerator in (3.8):

$$\pi_{\text{evid}}(\mathbf{y}|, \mathscr{P}_j, \mathscr{M}) = \int_{\Theta_j} \pi_{\text{like}}(\mathbf{y} | \boldsymbol{\theta}_j, \mathscr{P}_j, \mathscr{M}) \pi_{\text{prior}}(\boldsymbol{\theta}_j | \mathscr{P}_j, \mathscr{M}) d\boldsymbol{\theta}_j. \tag{3.9}$$

We next observe that the evidence (3.9) can be viewed as a likelihood for a discrete Bayesian calculation, yielding a new posterior called the posterior *model plausibility*, ρ_j,

$$\rho_j=\pi_{\text{post}}(\mathscr{P}_j|\mathscr{M},\mathbf{y})=\frac{\pi_{\text{evid}}(\mathbf{y}|,\mathscr{P}_j,\mathscr{M})\pi_{\text{prior}}(\mathscr{P}_j|\mathscr{M})}{\pi_{\text{evid}}(\mathscr{M}|\mathbf{y})},\quad 1\leq j\leq m. \tag{3.10}$$

Since $\{\rho_j\}$ is a probability distribution,

$$\sum_{j=1}^{m}\rho_j=1. \tag{3.11}$$

For given data **y**, the model with the largest plausibility is regarded as the best model in the set $\mathfrak{M}$.

Other methods of model selection are based on information theory. The most popular among these is the Akaike Information Criterion (AIC) (see Ref. 21):

$$\text{AIC}_j=-2\log\pi_{\text{like}}(\mathbf{y}|\hat{\boldsymbol{\theta}})+2k_j,\quad 1\leq j\leq m, \tag{3.12}$$

where π_{like} is the likelihood density, $\hat{\boldsymbol{\theta}}$ is the Maximum Likelihood Estimation (MLE) and k_j is the number of parameters in model $\mathscr{P}_j$. The Akaike weights are defined as:

$$w_j^{\text{AIC}}=\frac{\exp\{-\frac{1}{2}(\text{AIC}_j-\text{AIC}_{\min})\}}{\sum_{r=1}^{m}\exp\{-\frac{1}{2}(\text{AIC}_r-\text{AIC}_{\min})\}}. \tag{3.13}$$

Since $\sum_{r=1}^{m}w_r^{\text{AIC}}=1$, the Akaike weights play a similar role as the plausibilities ρ_j; the model(s) with the largest weights is (are) the best model among the set of models. Similarly, we can compute Bayesian Information Criterion (BIC):

$$\text{BIC}_j=-2\log\pi_{\text{like}}(\mathbf{y}|\hat{\boldsymbol{\theta}})+2k_j\log(n_d),\quad 1\leq j\leq m, \tag{3.14}$$

where n_d is the number of data points, herein $n_d=3$. The BIC weights:

$$w_j^{\text{BIC}}=\frac{\exp\{-\frac{1}{2}(\text{BIC}_j-\text{BIC}_{\min})\}}{\sum_{r=1}^{m}\exp\{-\frac{1}{2}(\text{BIC}_r-\text{BIC}_{\min})\}} \tag{3.15}$$

have the property $\sum_{r=1}^{m}w_r^{\text{BIC}}=1$, and thus, are alternative to the plausibilities and Akaike weights as indicators of the best model (see Ref. 21).

4. OPAL: The Occam Plausibility Algorithm

OPAL is a process for the systematic selection and validation of models in a given set $\mathfrak{M}$, given calibration observational data $\mathbf{y}_C$ and validation data $\mathbf{y}_V$.[12]

Briefly stated, OPAL consists of the following steps[12,25]:

1. A set $\mathfrak{M}$ of parametric models, as in (3.1), is identified, each with parameters $\boldsymbol{\theta}_i$ belonging to an appropriate parameter space Θ_i, $1 \leq i \leq m$.
2. A parameter sensitivity analysis is performed to assess the sensitivity of a model output function $Y(\boldsymbol{\theta})$ on perturbations in model parameters. Those models with parameters not appreciably affecting the output are eliminated, yielding a reduced set $\bar{\mathfrak{M}}$ of models,

$$\bar{\mathscr{M}} = \{\bar{\mathscr{P}}_1(\bar{\boldsymbol{\theta}}_1), \bar{\mathscr{P}}_2(\bar{\boldsymbol{\theta}}_2), \ldots, \bar{\mathscr{P}}_l(\bar{\boldsymbol{\theta}}_l)\}, \quad l \leq m.$$

3. The models surviving Step (2) are partitioned into "Occam Categories" according to their complexity. Those with the fewest parameters, for example, are put in Category 1; those with the next highest number of parameters in Category 2, and so forth.
4. Models in set $\mathfrak{M}^*$ of Category 1 are calibrated in calibration experiments involving calibration data $\mathbf{y}_C$, and the Bayesian statistical calibration calculation embodied in (3.3), yielding a calibrated set of Category 1 models,

$$\mathscr{M}^* = \{\mathscr{P}_1^*(\boldsymbol{\theta}_1^*), \mathscr{P}_2^*(\boldsymbol{\theta}_2^*), \ldots, \mathscr{P}_k^*(\boldsymbol{\theta}_k^*)\}.$$

5. The posterior Bayesian plausibilities ρ_i of all models in $\mathfrak{M}^*$ are computed for the calibration data $\mathbf{y}_C$ according to (3.10). Only the most plausible models with $\rho_i \geq \rho_j$, $i, j \leq k$ are retained.
6. An experimental validation scenario is constructed yielding validation observational data $\mathbf{y}_V$, and the most plausible model in Category 1 is used to compute a prediction of the observables $\mathbf{y}_V$; if the difference between the observables and the prediction measured in an appropriate metric or pseudo-metric is within a preset tolerance γ_{tol}, the model is deemed "valid". If not, one returns to Step (3) and repeats the process for the next category of models. If no models of any category are deemed valid, one returns to Step (1) and enlarges the set $\mathfrak{M}$ of possible model classes and then proceeds with the steps listed above.
7. Upon identifying a valid model, the forward problem is solved in the prediction scenario and the target QOI is computed, completing the prediction process.

All of these steps (see Fig. 2) are designed to cope with uncertainties in the choice of model, the model parameters, the observational data, and the target QOIs, all uncertainties generally characterized by probability densities.

5. Applications: Models of Tumor Growth

To demonstrate the theory and procedures presented this far, we consider two representative model classes in which tumor evolution depends on tumor cell net growth, diffusion and linear elastic deformation. The diffusive mechanisms are taken into account through both classical Fickian and generalized diffusion models.[8] The latter is driven by a gradient flow, characterized by an energy functional that encompasses diffusive gradients.

A key unknown scalar field in all of the models to be considered is the volume fraction $\boldsymbol{\phi}_T$ (= $\boldsymbol{\phi}_1$) of tumor cells. The displacement field is denoted by $\mathbf{u}$ and we assume that displacement gradient is small throughout the tissue domain Ω. Under these conditions, the infinitesimal deformation (strain) tensor is given by

$$\varepsilon(\mathbf{u})=\frac{1}{2}(\nabla\mathbf{u}+\nabla\mathbf{u}^t). \quad (5.1)$$

The strain tensor may be decomposed into the form

$$\varepsilon=\varepsilon^s+\varepsilon^g, \quad (5.2)$$

where $\boldsymbol{\varepsilon}^s$ and $\boldsymbol{\varepsilon}^g$ are the mechanical counterpart of strain (due to applied stress) and the stress-free strain (strain due to growth), respectively. The total free energy $\tilde{\Psi}$ of the system consists of a Ginzburg–Landau component depending only on the mixture species $\boldsymbol{\phi}_a$ ($\boldsymbol{\phi}_T$ in this case) and their gradients $\nabla\boldsymbol{\phi}_a$, and a stored energy potential W depending on the $\boldsymbol{\phi}_a$ and the strain measure $\boldsymbol{\varepsilon}(\mathbf{u})$. Thus, if $\tilde{\boldsymbol{\varepsilon}}$ is the energy per unit (spatial) volume, then:

$$\begin{aligned}\tilde{\Psi} &= \int_\Omega \tilde{\mathbf{e}}(\phi_T, \nabla\phi_T, \varepsilon(\mathbf{u}))d\mathbf{x},\\ \tilde{\mathbf{e}} &= \Psi(\phi_T, \nabla\phi_T)+W(\phi_T, \varepsilon(\mathbf{u})).\end{aligned} \quad (5.3)$$

The strain energy density is assumed to be of the form

$$W=\frac{1}{2}\varepsilon:\mathscr{C}(\phi_T)\varepsilon+\varepsilon:\overline{\mathbf{T}}(\phi_T), \quad (5.4)$$

where $\bar{\mathbf{T}}(\boldsymbol{\phi}_T)$ is a symmetric compositional stress tensor and

$$\mathscr{C}(\phi_T)=\mathscr{C}^h+g(\phi_T)(\mathscr{C}^t-\mathscr{C}^h) \quad (5.5)$$

is the linear elastic inhomogeneous material tensor. The function $g(\phi_T)$ allows $\mathscr{C}(\phi_T)$ to vary smoothly across the diffuse interface from the healthy tissue ($\mathscr{C}^h$) to the tumor tissue ($\mathscr{C}^t$). It is an interpolation function satisfying $g(\phi_T = 1) = 1$ and $g(\phi_T = 0) = 0$.[37,40]

The variational derivatives of the energy functional with respect to ϕ_T and $\boldsymbol{\varepsilon}$ define the chemical potential and the stress tensor, respectively. In line of (2.8), we have ($\alpha = 1$):

$$\mu_{\alpha\beta}=\mu_\alpha=\mu=\frac{\partial\Psi}{\partial\phi_T}-\nabla\cdot\frac{\partial\Psi}{\partial\nabla\phi_T}+\frac{\partial W(\phi_T,\boldsymbol{\varepsilon}(\mathbf{u}))}{\partial\phi_T}, \tag{5.6}$$

and

$$\begin{aligned}\mathbf{T}&=\det\mathbf{F}\mathbf{F}\left(2\frac{\partial W}{\partial\mathbf{C}}\right)\mathbf{F}^{-T}-\frac{\partial\Psi}{\partial\nabla\phi_T}\otimes\nabla\phi_T\\&=\frac{\partial W}{\partial\boldsymbol{\varepsilon}}-\frac{\partial\Psi}{\partial\nabla\phi_T}\otimes\nabla\phi_T,\end{aligned} \tag{5.7}$$

where the later equality results from the assumption of small deformations.

Because the diffusion mechanism occurs on a timescale much larger than that associated with inertia, we consider a quasi-static approximation and disregard inertial terms. Thus, the moment balance is simply given by

$$\nabla\cdot(\mathscr{C}(\phi_T)\boldsymbol{\varepsilon}+\overline{\mathbf{T}}(\phi_T))=0. \tag{5.8}$$

For the avascular tumor evolution considered here, we assume a linear isotropic compositional stress of the form $\bar{\mathbf{T}}(\phi_T) = \lambda\phi_T\mathfrak{A}$, where $\mathfrak{A}$ is the identity tensor and λ depends on the tumor growth rate. Thus, rewriting (5.8) in terms of the displacement vector $\mathbf{u}$, we obtain the mechanical equilibrium equation:

$$\frac{1}{2}\nabla\cdot[\mathscr{C}(\phi_T)(\nabla\mathbf{u}+\nabla\mathbf{u}^t)]=-\lambda\nabla\phi_T. \tag{5.9}$$

A major simplification occurs if we assume that the material is isotropic and homogeneous, in which case Hooke's law holds with the addition of a source term proportional to $\nabla\phi_T$:

$$0=\nabla\cdot G\nabla\mathbf{u}+\nabla\frac{G}{1-2\nu}(\nabla\cdot\mathbf{u})-\lambda\nabla\phi_T. \tag{5.10}$$

In (5.10), ν is the Poisson's ratio and $G=\frac{E}{2(1+\nu)}$ is the shear modulus, with E the Young's modulus. The definition of the free energy density $\Psi(\phi_T,\nabla\phi_T)$ yields the different tumor

growth models considered here. As a simplification, we assume constant mechanical properties throughout the whole domain.

5.1. The reaction–diffusion models

In this model family, the mass balance expresses the rate of change of the cancer cell population density due to Fickian diffusion and includes the net proliferation of cancer cells.[41] The latter is modeled by a logistic law and the former may be derived by assuming that the total energy functional (5.3) is given by the internal energy of the system: i.e. $\tilde{e}=c\phi_T^2/2$. Then, the chemical potential is simply given by $\mu = c\boldsymbol{\phi}_T$, yielding the reaction–diffusion (RD) model:

$$\frac{\partial \phi_T}{\partial t}=\nabla \cdot M_T^* \nabla \phi_T+\lambda_T^{\mathrm{grow}} \phi_T(1-\phi_T), \tag{5.11}$$

in which $M_T^*=cM_T$ is the diffusion coefficient.

If we assume that the total energy functional (5.3) is given by the internal energy of the system plus the strain energy density we get

$$\tilde{\Psi}=\int_\Omega \left[\frac{c}{2}\phi_T^2+\frac{1}{2}\varepsilon:\mathscr{C}(\phi)\varepsilon+\varepsilon:\lambda\phi\mathscr{I}\right] d\mathbf{x}. \tag{5.12}$$

Under these hypotheses, we get the reaction–diffusion model with mechanical coupling (MD):

$$\begin{cases} \frac{\partial \phi_T}{\partial t}=\nabla \cdot M_T \nabla \mu+\lambda_T^{\mathrm{grow}} \phi_T(1-\phi_T); \\ \mu=c\phi_T-\lambda\nabla \cdot \mathbf{u}. \end{cases} \tag{5.13}$$

The complete RD and MD models incorporating the mechanical deformation effects are obtained by including the mechanical equilibrium equation (5.10).

5.2. The phase-field models

The phase-field modeling approach considered here is derived from the models developed in Ref. 24. We assume that the tumor microenvironment is a mixture of tumor and healthy tissue. For this two-constituent medium, $\boldsymbol{\phi}_T$ is scaled so that $0 \leq \boldsymbol{\phi}_T \leq 1$, in which the upper and lower bounds represent the tumor and healthy tissue volume fractions, respectively, separated by a typically thin interface where $0 < \boldsymbol{\phi}_T < 1$. The system dynamics is driven by the following energy functional,

$$\tilde{\Psi}=\int_{\Omega}\left[\overline{E}\phi_T^2(1-\phi_T)^2+\frac{\varepsilon_T^2}{2}|\nabla\phi_T|^2+\frac{1}{2}\boldsymbol{\varepsilon}:\mathscr{C}(\phi_T)\boldsymbol{\varepsilon}+\boldsymbol{\varepsilon}:\lambda\phi_T\mathscr{I}\right]d\mathbf{x}, \quad (5.14)$$

which includes the bulk energy density due to local interactions (first term), the interfacial energy density (second term) and the strain energy density (third and fourth terms). The positive constants $\bar{E}$ and ε_T are energy scales of the bulk phase and interface, respectively. As shown before, the quasi-static mechanical equilibrium is modeled by (5.10). Assuming again a logistic tumor growth (recall Eqs. (2.8) and (2.9)), the mass balance yields the Phase-Field (PF) model:

$$\begin{cases}\frac{\partial\phi_T}{\partial t}=\nabla\cdot M_{\mathrm{PF}}(\phi_T)\nabla\mu+\lambda_T^{\mathrm{grow}}\phi_T(1-\phi_T);\\ \mu=2\overline{E}\phi_T(1-3\phi_T+2\phi_T^2)-\varepsilon_T^2\Delta\phi_T-\lambda\nabla\cdot\mathbf{u}.\end{cases} \quad (5.15)$$

Here, we assume a nonlinear tumor cell mobility in the form $M_{\mathrm{PF}}=M_T\phi_T^2(1-\phi_T)^2$ so that it vanishes wherever there is either only tumor or healthy cells. We note that (5.15) implicitly takes into account the deformation on the tumor evolution.

5.3. Deformation feedback on the tumor growth

The stress field developed due to tumor growth affects the cell behavior as well as a large variety of cross-talk signals in the microenvironment. Experimental studies[6,16,34] have shown that the accumulation of compressible stresses inside tumors inhibits tumor growth while tensile stress can squeeze blood and lymphatic vessels, decreasing fluid flow and eventually increasing tumor aggressiveness. In this work, we are particularly interested in the mechanical aspects of the tumor growth regarding their link with tumor cell proliferation and motility. We hypothesize that mechanical stresses inhibit tumor growth by damping the mobility coefficient or the net rate growth. The damping strength is regulated by the stress measure Σ and a scaling constant γ in the form

$$d=\exp(-\gamma\textstyle\sum). \quad (5.16)$$

Thus, we consider three cases: $M_T:=\exp(-\gamma\Sigma)M_T$; $M_T^*:=\exp(-\gamma\sum)M_T^*$; and $\lambda_T^{\mathrm{grow}}:=\exp(-\gamma^{\mathrm{grow}}\sum)\lambda_T^{\mathrm{grow}}$. Here we take for the stress measure,[41] Σ, the Von Mises stress,

$$\sigma_{\mathrm{VM}}=\sqrt{\frac{1}{2}[(\sigma_{xx}-\sigma_{yy})^2+(\sigma_{yy}-\sigma_{zz})^2+(\sigma_{zz}-\sigma_{xx})^2+6(\sigma_{xy}^2+\sigma_{xz}^2+\sigma_{zx}^2)]}.$$

6. A Representative Set $\mathfrak{M}$ of Parametric Classes of Tumor Growth Models

We employ the OPAL framework[12] for model selection and validation of all tumor growth parametric model families introduced in the preceding section. The OPAL framework brings together model calibration, determination of sensitivities of outputs to parameter variances, and calculation of model plausibilities for model selection. We identify the model classes and perform sensitivity analyses of the QOI, here chosen as the tumor volume as a function of time or tumor area for 2D depictions obtained from *in vivo* magnetic resonance imaging data.

Table 2 summarizes a set of possible models derived from the previous models where: PF# = phase-field model; RD# = reaction–diffusion model without mechanical coupling and MD# = reaction–diffusion model with mechanical coupling. We indicate with ✓ if the model contains the parameter or variable; otherwise, we leave the cell empty. All models include variable tumor volume fraction ϕ_T, a diffusional/mobility and the net growth rate λ_T^{grow}. Likewise, all models that include mechanical deformation consider the elastic parameters G and ν, and the compositional growth strength λ. We remark that the phase-field models involve the parameters related to the energy scales ($\bar{E}$ and ε_T). The models are classified into Occam's categories according to their number of parameters: the model with fewest parameters is assigned to Category 1.

7. Numerical Simulation

The scenario that is used for model calibration, validation and prediction is based on data that were obtained in the murine model of glioma growth in Ref. 17. We are using the data from just one animal, after the first 10 days of tumor growth, it was imaged with Diffusion Weighted Magnetic Resonance Imaging (DW-MRI) during an interval of 10 days. With the time relative to the date of tumor implantation, data were collected on the 10th, 12th, 14th, 15th, 16th, 18th and 20th days. The MRI domain encompasses 41×61×16 voxels, each one having 250×250×100 μm. In our work we selected the 12th DW-MRI slice, where the tumor is observed during all measurements. In Fig. 3, the domain obtained from the MRI is presented with the QOI, the area of the tumor, in red.

For the calibration scenario we selected days 10, 12, 14 and 15, where the 10th day is used as an initial condition. During the validation step, the initial condition is the glioma at $t = 15$ day and days 16 and 18 are used in order to update the PDF of the parameters. Usually, for the prediction, the QOI is an unknown. However, in order to illustrate the capabilities of the selected model, we left out day 20 to compare with the outcome of our model. We use as an initial condition the 18th day in order to predict the tumor area at the 20th day.

All models were implemented in C++ under the *libMesh* framework.[20] The total simulation time, including calibration, validation and prediction of each model, requires 10 h on 24 processors on the Lonestar 5 Cluster, at the Texas Advanced Computing Center (TACC) of The University of Texas at Austin (http://www.tacc.utexas.edu). The mesh is constructed based on a voxel representation of the brain (see Fig. 4) and the time step is $\Delta t = 0.05$ days.

For model calibration and validation, we employ a multi-level Monte Carlo algorithm (see Ref. 29) that is available in the library QUESO.[30]

The calibration priors are assumed to have uniform distributions, as presented in Table 3. We select the range in order to contain the values calibrated for this data by Ref. 17. The same priors are used for all the simulated models.

7.1. Sensitivity analysis

In order to investigate the effects of uncertain input parameters in the tumor growth models, we use the elementary effects method for the sensitivity analysis. The domain is the same in Fig. 4 and the initial conditions are taken from the 10th day data exhibited in Fig. 3. We conduct the simulation until $t = 20$ days and $N_t = 50$ trajectories for each model. The total number of simulations run is given by $N_t \times$(#Params+1). Table 4 shows the results for all the models in $\mathfrak{M}$. Clearly, the area of the tumor is more sensitive to the rate of tumor growth. Despite the influence of some of the parameters being very small (on the order of 10^{-7}), we retain all the models for the next OPAL steps.

7.2. Model calibration and validation using MCMC

First we evaluate the model in Occam Category 1. Model RD01 is a reaction–diffusion model without mechanical deformation, so we only need to calibrate the parameters M_T^* and λ_T^{grow}. In Fig. 5, the prior and posterior PDF to each parameter is presented.

As in Category 1 we have just one model, the plausibility step is not necessary, so we can move forward to the validation step. At the validation step, the posterior from the calibration step is used as a prior to the validation step in order to update our knowledge regarding the parameters. In Fig. 6, the prior and posterior for the validation step are exhibited. Using this new posterior, the forward problem is solved using Monte Carlo sampling and the PDF for the area of the tumor is computed. The error between the *in vivo* data and the model simulation is given by the Kullback–Leibler divergence divided by the variance of the data. In order to be declared not invalid, $D_{\text{KL}}/\sigma_t^2 = D_{\text{KL}}(\sigma_t^2) \leq \gamma_{\text{tol}} = 0.7$, where σ_t^2 is the variance at time t. Both the choice of a measure of accuracy (the $D_{\text{KL}}(\sigma_t^2)$) and the tolerance ($\gamma_{\text{tol}}$) are subjective choices. The D_{KL} is a common measure of relative entropy between probability distributions and is a natural choice in the present setting. The tolerance is a subjective threshold picked to generally correspond to relatively close agreement (within 10–15%) of the tumor mass (area) observed and that predicted by the model. The model RD01 has $D_{\text{KL}}(\sigma_{16}^2) = 0.92$ and $D_{\text{KL}}(\sigma_{18}^2) = 0.70$, so, the model is not valid.

The next step is to proceed to the model in Occam Category 2, which is also not valid. In Category 3, we have three models with six parameters each. So, after the calibration step we compute the plausibility of each model. The most plausible model, in this case model MD01, is selected for the validation step. Even though model MD01 is the most plausible, it is not a valid model. We continue the simulation until a not invalid model is selected.

Table 5 presents the results for all the simulations performed. For this specific dataset, model PF04 from Category 5 satisfies the prescribed tolerance, with $D_{\mathrm{KL}}(\sigma_{16}^2)=0.70$ and $D_{\mathrm{KL}}(\sigma_{18}^2)=0.66$. In Fig. 7 we compare the mean results for the tumor area at times 16 and 18 days with their respective *in vivo* data. It is possible to conclude that model PF04, which is a phase-field model that includes the mechanical deformation feedback at the tumor growth rate ($\lambda_T^{\mathrm{grow}}$), is not invalid. As the model PF04 is already *not* invalid, it is not necessary to run the more complex model PF05.

Using the validation posterior for the parameters from model PF04, an example of the prediction of the model is presented in Fig. 8. As can be seen, the model is able to predict the area of the tumor with 9.75% difference from the mean value.

For the next experiment, we replace the plausibility as the tool to select the best model among the ones from the same Occam Category, by the AIC weights and the BIC weights. These results are presented in Table 6, where the best model is now PF03 for both methods. The AIC and BIC weights have the same value, for all the models, as the number of data points is the same ($n_d = 3$) and the number of parameters is the same for the models within the same Occam Category. Due to the fact that we are computing $\log \pi_{\mathrm{like}}(\mathbf{y}/\hat{\boldsymbol{\theta}})$ numerically using 10^4 samples, the computation of the maximum value presents numerical errors. This is evident in the fact that different models are selected as the best from their Occam Category.

The plausibility calculation indicates that MD01 is the best among the models in Occam Category 3 and PF04 is the best among Category 5. However, when using AIC or BIC weights, the best models for Categories 3 and 5 are RD02 and PF03, respectively. This result can be justified by the differences in AIC and BIC given by:

$$\begin{aligned}\mathrm{AIC}_{\mathrm{RD02}}-\mathrm{AIC}_{\mathrm{MD01}}&=\mathrm{BIC}_{\mathrm{RD02}}-\mathrm{BIC}_{\mathrm{MD01}}=0.34,\\ \mathrm{AIC}_{\mathrm{PF03}}-\mathrm{AIC}_{\mathrm{PF04}}&=\mathrm{BIC}_{\mathrm{PF03}}-\mathrm{BIC}_{\mathrm{PF04}}=0.21.\end{aligned}$$

As indicated in Ref. 19, if the difference is below 0.5, the evidence against the higher AIC or BIC is insignificant.

8. Conclusions

In this work, we employ the OPAL framework for model selection and validation to study a large body of tumor growth models. We develop/select 13, thermodynamically consistent, continuum tumor growth models, five of them using the phase-field modeling approach and the others being reaction–diffusion type models. The proposed models are able to reproduce the tumor growth patterns approximating those observed during *in vivo* experiments. The goal is, following Occam's Razor, to choose the best and simplest model, simplest meaning the one with fewest parameters.

We demonstrate that the OPAL is able to assist in the selection of the best tumor growth model from a defined set of models. The methodologies and results confirm that the OPAL strategy provides a powerful framework for model selection, parameter estimation, and model validation in the presence of uncertainties. The use of a Bayesian framework for

calibration and validation makes possible the characterization of probability densities depicting all relevant parameters.

As a tool to select the best model among the same Occam Category, we use either the model plausibility, the AIC weights or the BIC weights. As expected, the AIC and BIC weights lead to the same result, indicating in our application example that the model PF03 is the best model. However, when we use the posterior plausibility measure, the model selected as the best is the PF04. We can conclude that the best approach, for these data and with the tumor area as a QOI, is to use a phase-field model with a deformation feedback, either in the mobility or the tumor growth rate.

The extension of this study to different scenarios including (for example) radiotherapy and chemotherapy treatments, and more refined QOIs that take into account (for example) the shape and connectivity of the tumor and the number of cells per voxel, is the target of future work.

Acknowledgments

Oden and Lima acknowledge early support of their work on tumor growth models by the National Science Foundation under Grant DMS 1115865. Their work on predictive modeling and uncertainty quantification is supported by US Department of Energy Office of Science, Office of Advanced Scientific Computing Research, Applied Mathematics Program under Award Number DE-5C0009286. Almeida acknowledges support of the National Counsel of Technological and Scientific Development (CNPq) 305612/2013-1. We also thank CPRIT for funding through RR160005 and the NCI for funding through U01CA174706 and R01CA186193.

References

1. Beck JL. Bayesian system identification based on probability logic. Struct Control Health Monit. 2010; 17:825–847.
2. Bellomo N, Bellouquid A, Tao Y, Winkler M. Toward a mathematical theory of Keller–Segel models of pattern formation in biological tissues. Math Models Methods Appl Sci. 2015; 25:1663–1763.
3. Bellomo N, Li NK, Maini PK. On the foundations of cancer modelling: Selected topics, speculations, and perspectives. Math Models Methods Appl Sci. 2008; 18:593–646.
4. Bowen, RM. Theory of mixtures. In: Eringen, AC., editor. Continuum Physics III. Academic Press; 1976.
5. Box, GEP. Robustness in Statistics. Academic Press; 1979. Robustness in the strategy of scientific model building; p. 201-236.
6. Cheng G, Tse J, Jain RK, Munn LL. Micro-environmental mechanical stress controls tumor spheroid size and morphology by suppressing proliferation and inducing apoptosis in cancer cells. PLoS One. 2009; 4:e4632. [PubMed: 19247489]
7. Chow GC. A comparison of the information and posterior probability criteria for model selection. J Econometrics. 1981; 16:21–33.
8. Cohen DS, Murray JD. A generalized diffusion model for growth and dispersal in a population. J Math Biol. 1981; 12:237–249.
9. Cristini, V., Lowengrub, J. Multiscale Modeling of Cancer: An Integrated Experimental and Mathematical Modeling Approach. Cambridge Univ. Press; 2010.
10. Deisboeck, TS., Stamatakos, GS. Chapman & Hall/CRC Mathematical and Computational Biology. Taylor & Francis; 2010. Multiscale Cancer Modeling.
11. Eringen AC, Ingram JD. A continuum theory of chemically reacting media — I. Int J Engrg Sci. 1965; 3:197–212.
12. Farrell K, Oden JT, Faghihi D. A Bayesian framework for adaptive selection, calibration, and validation of coarse-grained models of atomistic systems. J Comput Phys. 2015; 295:189–208.

13. Hanahan D, Weinberg RA. The hallmarks of cancer. Cell. 2000; 100:57–70. [PubMed: 10647931]
14. Hanahan D, Weinberg RA. Hallmarks of cancer: The next generation. Cell. 2011; 144:646–674. [PubMed: 21376230]
15. Hawkins-Daarud A, Prudhomme S, van der Zee KG, Oden JT. Bayesian calibration, validation, and uncertainty quantification of diffuse interface models of tumor growth. J Math Biol. 2013; 67:1457–1485. [PubMed: 23053536]
16. Helmlinger G, Netti PA, Lichtenbeld HC, Melder RJ, Jain RK. Solid stress inhibits the growth of multicellular tumor spheroids. Nature Biotechnol. 1997; 15:778–783. [PubMed: 9255794]
17. Hormuth DA II, Weis JA, Barnes SL, Miga MI, Rericha EC, Quaranta V, Yankeelov TE. Predicting *in vivo* glioma growth with the reaction diffusion equation constrained by quantitative magnetic resonance imaging data. Phys Biol. 2015; 12:046006. [PubMed: 26040472]
18. Jeffreys, H. The Theory of Probability. 3. Oxford Univ. Press; 1998.
19. Kass RE, Raftery AE. Bayes factors. J Amer Statist Assoc. 1995; 90:773–795.
20. Kirk BS, Peterson JW, Stogner RH, Carey GF. libMesh: A C++ library for parallel adaptive mesh refinement/coarsening simulations. Engrg Comput. 2006; 22:237–254.
21. Konishi, S., Kitagawa, G. Information Criteria and Statistical Modeling. 1. Springer-Verlag; 2008.
22. Le Maître, OP., Knio, OM. Spectral Methods for Uncertainty Quantification. Springer; 2010.
23. Lima EABF, Almeida RC, Oden JT. Analysis and numerical solution of stochastic phase-field models of tumor growth. Numer Methods Partial Differential Equations. 2015; 31:552–574.
24. Lima EABF, Oden JT, Almeida RC. A hybrid ten-species phasefield model of tumor growth. Math Models Methods Appl Sci. 2014; 24:2569–2599.
25. Oden, JT., Babuska, I., Faghihi, D. Encyclopedia of Computational Mechanics. John Wiley & Sons; Predictive computational science: Computer predictions in the presence of uncertainty. to appear
26. Oden JT, Hawkins A, Prudhomme S. General diffuse-interface theories and an approach to predictive tumor growth modeling. Math Models Methods Appl Sci. 2010; 20:477–517.
27. Oden JT, Lima EABF, Almeida RC, Feng Y, Rylander MN, Fuentes D, Faghihi D, Rahman MM, DeWitt M, Gadde M, Zhou JC. Toward predictive multiscale modeling of vascular tumor growth. Arch Comput Methods Engrg. 2015; doi: 10.1007/s11831-015-9156-x
28. Oden JT, Prudencio EE, Hawkins-Daarud A. Selection and assessment of phenomenological models of tumor growth. Math Models Methods Appl Sci. 2013; 23:1309–1338.
29. Prudencio E, Cheung SH. Parallel adaptive multilevel sampling algorithms for the Bayesian analysis of mathematical models. Int J Uncertain Quant. 2012; 2:215–237.
30. Prudencio, EE., Schulz, KW. Euro-Par 2001 Workshops. Springer; 2012. The parallel C++ statistical library “QUESO”: Quantification of uncertainty for estimation, simulation and optimization; p. 398-407.
31. Rajagopal, KR., Tao, L. Mechanics of Mixtures. World Scientific; 1995.
32. Saltelli, A., Chan, K., Scott, E. Wiley Paperback Series. Wiley; 2009. Sensitivity Analysis.
33. Saltelli, A., Ratto, M., Andres, T., Campolongo, F., Cariboni, J., Gatelli, D., Saisana, M., Tarantola, S. Global Sensitivity Analysis: The Primer. John Wiley & Sons; 2008.
34. Stylianopoulos T, Martin JD, Chauhan VP, Jain SR, Diop-Frimpong B, Bardeesy N, Smith BL, Ferrone CR, Hornicek FJ, Boucher Y, Munn LL, Jain RK. Causes, consequences, and remedies for growth-induced solid stress in murine and human tumors. Proc Natl Acad Sci. 2012; 109:15101–15108. [PubMed: 22932871]
35. Truesdell C. Mechanical basis of diffusion. J Chem Phys. 1962; 37:2336–2344.
36. Truesdell, C., Toupin, R. Handbuch der Physik. Springer-Verlag; 1960. The classical field theories.
37. Tsukada Y, Murata Y, Koyama T, Morinaga M. Phase-field simulation of the effect of elastic inhomogeneity on microstructure evolution in Ni-based superalloys. Mater Trans. 2009; 50:744–748.
38. Weis JA, Miga MI, Arlinghaus LR, Li X, Chakravarthy AB, Abramson V, Farley J, Yankeelov TE. A mechanically coupled reaction–diffusion model for predicting the response of breast tumors to neoadjuvant chemotherapy. Phys Med Biol. 2013; 58:5851–5866. [PubMed: 23920113]

39. Weis JA, Miga MI, Li X, Arlinghaus LR, Abramson VG, Chakravarthy AB, Farley J, Yankeelov TE. Predicting the response of breast cancer to neoadjuvant chemotherapy using a mechanically coupled reaction–diffusion model. Cancer Res. 2015; 75:4697–4707. [PubMed: 26333809]
40. Wise SM, Lowengrub JS, Frieboes HB, Cristini V. Three-dimensional multispecies nonlinear tumor growth: Model and numerical method. J Theor Biol. 2008; 253:524–543. [PubMed: 18485374]
41. Yankeelov TE, Atuegwu N, Hormuth D, Weis JA, Barnes SL, Miga MI, Rericha EC, Quaranta V. Clinically relevant modeling of tumor growth and treatment response. Sci Trans Med. 2013; 5:187ps9.
42. Yankeelov TE, Quaranta V, Evans KJ, Rericha EC. Toward a science of tumor forecasting for clinical oncology. Cancer Res. 2015; 75:918–923. [PubMed: 25592148]

Fig. 1.

A representation of the eight Hallmarks of Cancer discussed in Refs. 12 and 13. *Sustaining proliferative signaling*: the ability to divide even without the presence of growth factor or a hyper-response to these signals; *Deregulating cellular energetics*: the ability to reprogram cellular glucose metabolism, and thus cellular energy production; *Resisting cell death*: acquired resistance to signals that lead to cell death (apoptosis); *Inducing angiogenesis*: the ability to induce the growth of new blood vessels when the cells have a low level of nutrients and oxygen; *Evading growth suppressors*: the ability to ignore antiproliferative signals that maintain cellular quiescence; *Avoiding immune destruction*: the ability of cancer cells to evade the attack and destruction by the immune system; *Enabling replicative immortality*: the ability to ignore the replicative senescence (cellular old age); *Activating invasion and metastasis*: the ability to spread to other parts of the body and form secondary tumors.

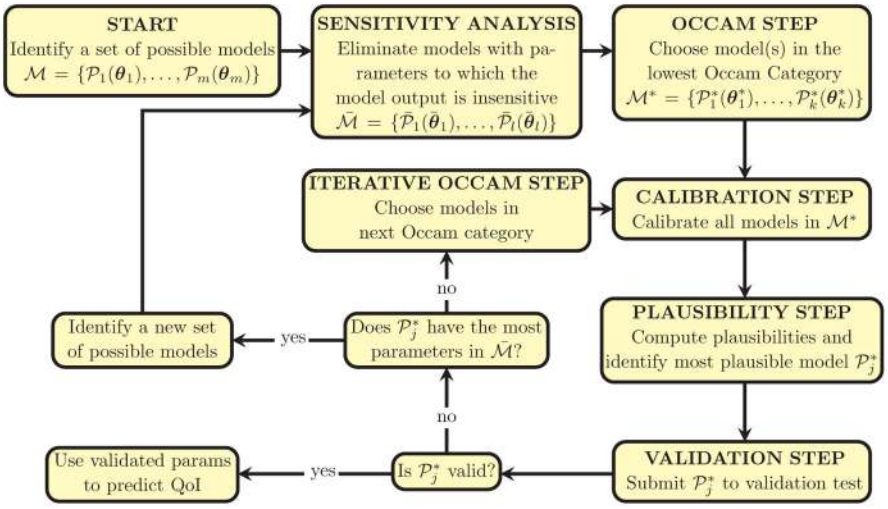

Fig. 2.
The OPAL.

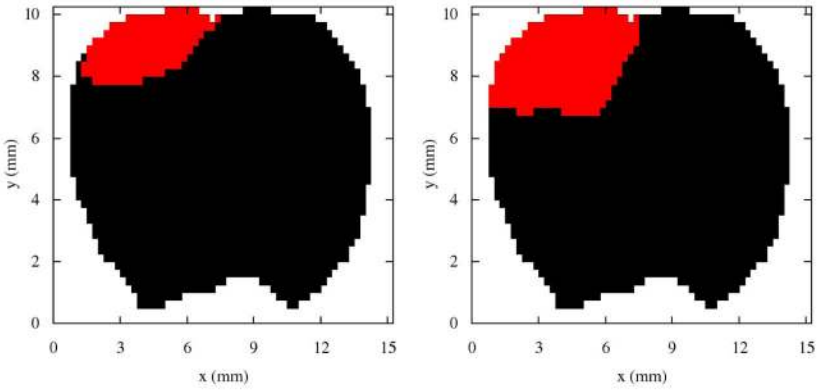

(a) 10th day (b) 12th day

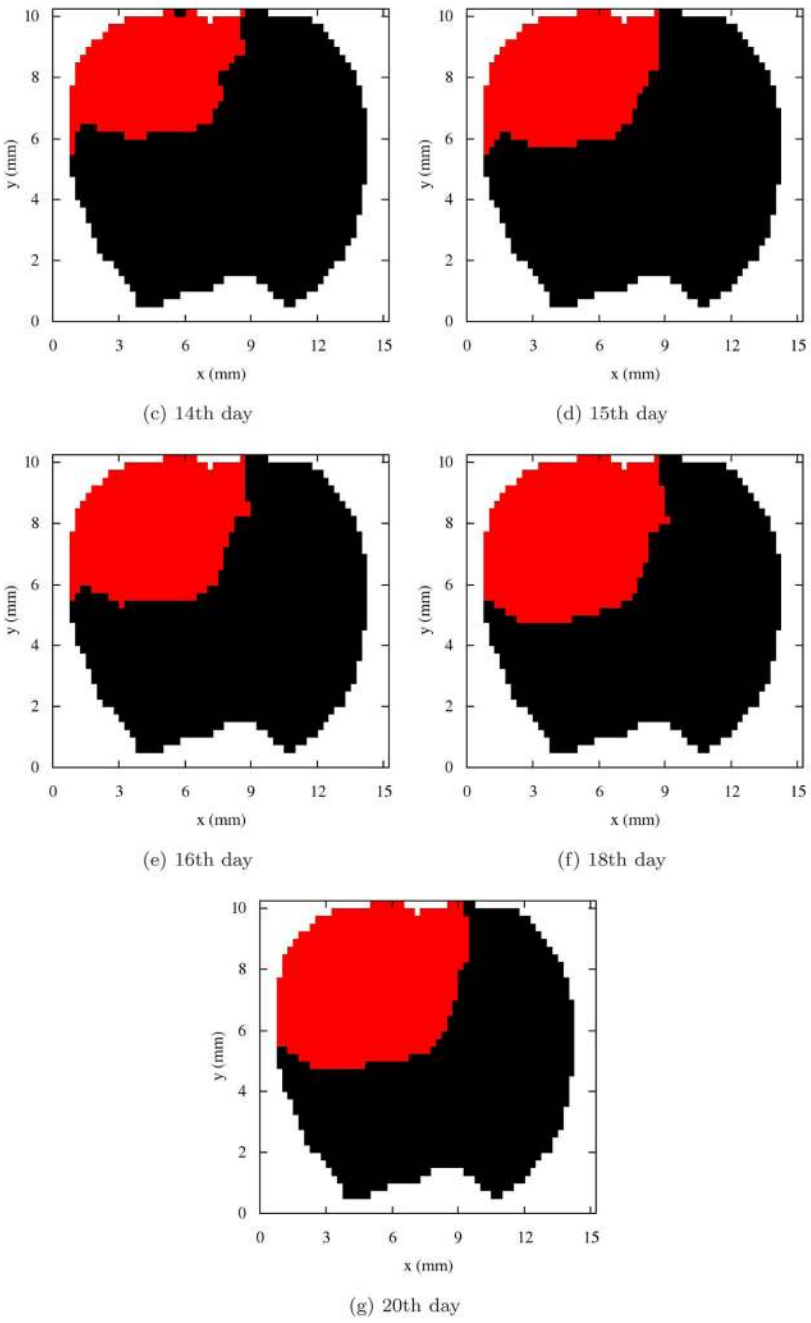

Fig. 3.
Observational data extracted from MRI images of progressive tumor growth in a murine experiment.[16]

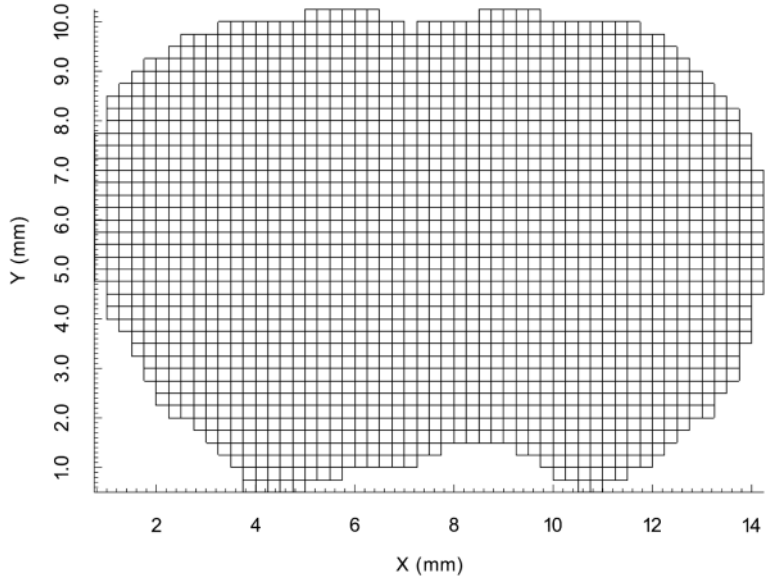

Fig. 4.
Voxels from the MRI that capture the domain of the brain.

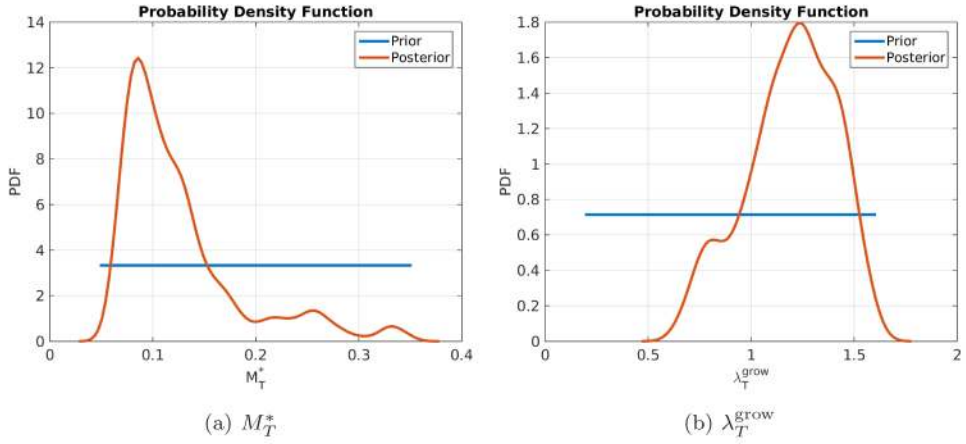

(a) M_T^* (b) $\lambda_T^{\mathrm{grow}}$

Fig. 5.

Prior $(\pi^C_{\mathrm{prior}}(\boldsymbol{\theta}_1|\mathscr{P}_1,\mathscr{M}))$ and posterior $(\pi^C_{\mathrm{post}}(\boldsymbol{\theta}_1|\mathbf{y}_C,\mathscr{P}_1,\mathscr{M}))$ for model RD01 at the calibration step.

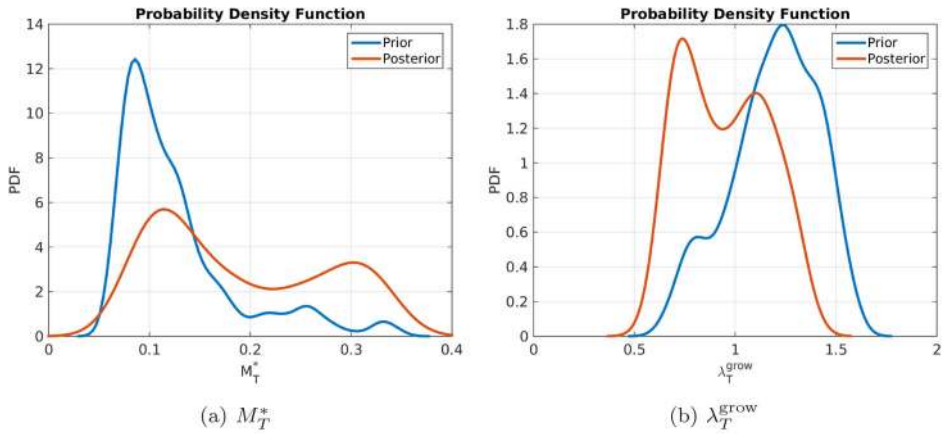

(a) M_T^* (b) $\lambda_T^{\mathrm{grow}}$

Fig. 6.

Prior $(\pi^V_{\mathrm{prior}}(\boldsymbol{\theta}_1|\mathscr{P}_1,\mathscr{M}))$ and posterior $(\pi^V_{\mathrm{post}}(\boldsymbol{\theta}_1|\mathrm{y}_V,\mathscr{P}_1,\mathscr{M}))$ for model RD01 at the validation step.

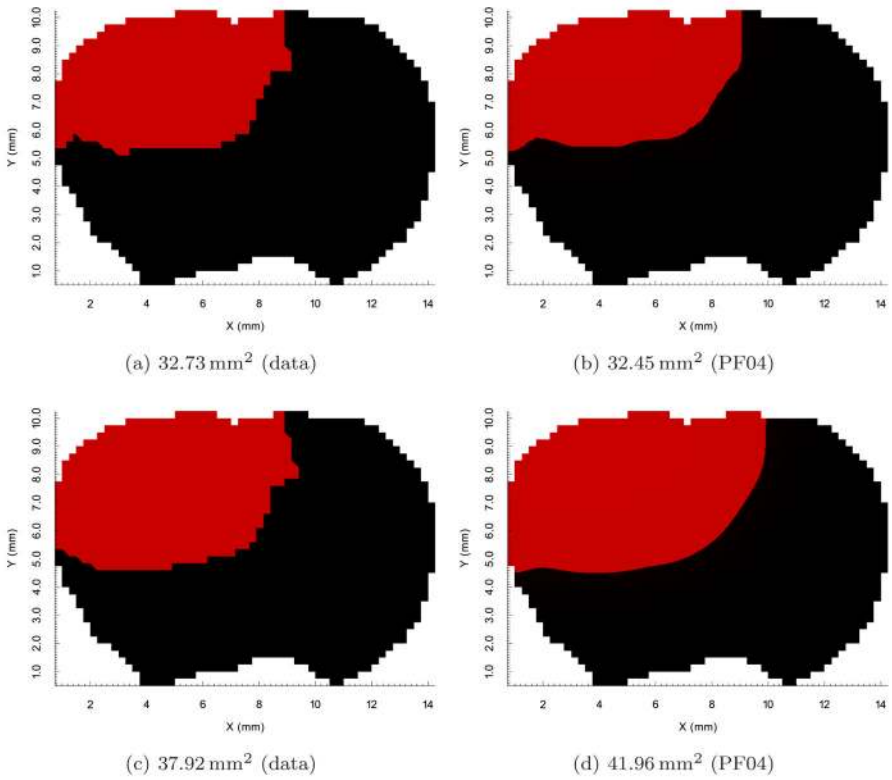

Fig. 7.
Tumor area evolution at slice 12 at $t = 16$ (a) and (b) and $t = 18$ (c) and (d).

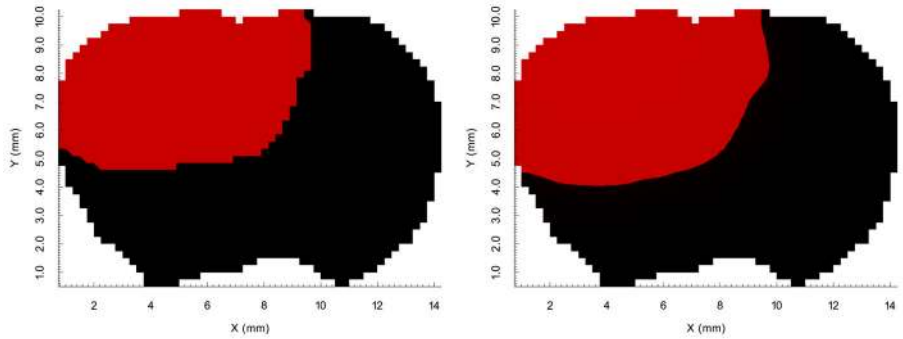

(a) $40.92\,\mathrm{mm}^2$ (data) (b) $44.91\,\mathrm{mm}^2$ (PF04)

Fig. 8.
Tumor area evolution at slice 12 ($t = 20$).

Table 1

Nomenclature for the ath species in an N-species mixture.

ϕ_a	Volume fraction
ρ_a	Mass density of ath constituent ($\rho(\mathbf{x},t)=\sum_{\alpha=1}^{N}\rho_\alpha\phi_\alpha$)
$\mathbf{v}_a$	Velocity field in ath constituent ($\mathbf{v}(\mathbf{x},t)=\rho^{-1}\sum_{\alpha=1}^{N}\rho_\alpha\phi_\alpha\mathbf{v}_\alpha$)
$\rho_a S_a$	Mass supplied to ath constituent by other constituents
$\rho_a\mathbf{J}_a$	Mass flux entering ath constituent from other constituents
$\mathbf{T}_a$	Partial Cauchy stress tensor
$\mathbf{m}_a$	Intrinsic moment of momentum
$\hat{\mathbf{p}}_a$	Momentum supplied by other constituents
$\mathbf{b}_a$	Body force ($\mathbf{b}=\sum_{\alpha=1}^{N}\rho_\alpha\phi_\alpha\mathbf{b}_\alpha$)
$\mathbf{L}_a$	Velocity gradient tensor = $\nabla\mathbf{v}_a$
$\hat{\varepsilon}_a$	Energy supplied by other constituents
Υ_a	Energy supplied by changes in surface tensions and concentrations of nutrient reactions
η_a	Entropy density ($\eta(\mathbf{x},t)=\sum_{\alpha=1}^{N}\rho_\alpha\phi_\alpha\eta_\alpha$)
$\mathbf{H}_a$	Entropy flux
Γ_a	$\rho_\alpha^{-1}(S_\alpha-\nabla\cdot\mathbf{J}_\alpha)$

Table 2

Initial set of possible models.

Model	Variables			Parameters											# Params	Occam
	ϕ_T	μ	u	M_T	M_T^*	c	λ_T^{grow}	$\bar{E}_T$	e_T	E	ν	λ	γ	γ^g		Category
RD01	✓				✓		✓								2	1
PF01	✓	✓		✓			✓	✓	✓						4	2
RD02	✓		✓		✓		✓			✓	✓	✓	✓		6	3
RD03	✓		✓		✓		✓			✓	✓	✓		✓	6	3
MD01	✓	✓	✓	✓		✓	✓			✓	✓	✓			6	3
RD04	✓		✓		✓		✓			✓	✓	✓	✓	✓	7	4
MD02	✓	✓	✓	✓		✓	✓			✓	✓	✓	✓		7	4
MD03	✓	✓	✓	✓		✓	✓			✓	✓	✓		✓	7	4
PF02	✓	✓	✓	✓			✓	✓	✓	✓	✓	✓			7	4
MD04	✓	✓	✓	✓		✓	✓			✓	✓	✓	✓	✓	8	5
PF03	✓	✓	✓	✓			✓	✓	✓	✓	✓	✓	✓		8	5
PF04	✓	✓	✓	✓			✓	✓	✓	✓	✓	✓		✓	8	5
PF05	✓	✓	✓	✓			✓	✓	✓	✓	✓	✓	✓	✓	9	6

Math Models Methods Appl Sci. Author manuscript; available in PMC 2017 November 01.

Table 3

Calibrated parameters and their priors.

Parameter	Prior
M_T	$\mathcal{U}(0.2, 1.0)$
M_T^*	$\mathcal{U}(0.05, 0.35)$
c	$\mathcal{U}(0.1, 0.55)$
λ_T^{grow}	$\mathcal{U}(0.2, 1.6)$
$\bar{E}_T$	$\mathcal{U}(0.15, 0.35)$
e_T	$\mathcal{U}(0.5, 0.7)$
E	$\mathcal{U}(1.2, 2.8)$
ν	$\mathcal{U}(0.2, 0.49)$
λ	$\mathcal{U}(0.001, 0.004)$
γ	$\mathcal{U}(80, 320)$
γ^g	$\mathcal{U}(80, 320)$

Table 4

Sensitivity analysis for models $\mathcal{P}_1$ to $\mathcal{P}_{13}$.

Model	Sensitivity of the parameters (μ^*)										
	M_T	M_T^*	c	λ_T^{grow}	$\bar{E}_T$	e_T	E	ν	λ	γ	γ^g
RD01		19.49		34.74							
PF01	2.59			32.05	0.08	2.63					
RD02		22.06		32.13			3.24×10^{-5}	0.55	1.28	1.41	
RD03		21.01		30.53			2.63×10^{-5}	0.68	2.44		2.65
MD01	20.71		15.70	33.86			2.97×10^{-5}	7.89×10^{-5}	9.54×10^{-5}		
RD04		16.63		29.94			3.02×10^{-5}	1.37	3.72	1.21	2.55
MD02	14.88		15.88	31.75			5.40×10^{-5}	0.74	1.57	1.37	
MD03	14.05		14.93	29.91			4.23×10^{-5}	0.91	2.79		2.48
PF02	2.77			32.02	0.08	3.21	9.00×10^{-7}	2.40×10^{-6}	5.70×10^{-6}		
MD04	12.03		16.32	28.61			2.64×10^{-5}	1.31	3.23	0.95	1.81
PF03	2.89			32.21	0.07	3.60	9.00×10^{-7}	0.16	0.46	0.39	
PF04	2.61			27.74	0.07	3.17	9.00×10^{-7}	0.65	3.20		3.02
PF05	2.46			25.86	0.06	2.86	1.80×10^{-6}	0.44	3.24	0.34	2.39

Math Models Methods Appl Sci. Author manuscript; available in PMC 2017 November 01.

Table 5

Results for the OPAL framework using the plausibility for model selection.

Model	Occam category	Plausibility	$D_{\mathrm{KL}}(\sigma_{16}^2)$	$D_{\mathrm{KL}}(\sigma_{18}^2)$
RD01	**1**	n/a	0.92	0.70
PF01	**2**	n/a	0.65	0.74
RD02	**3**	0.22		
RD03	**3**	0.14		
MD01	**3**	0.64	0.93	0.72
RD04	**4**	0.02		
MD02	**4**	0.06		
MD03	**4**	0.02		
PF02	**4**	0.90	0.68	0.76
MD04	**5**	0.02		
PF03	**5**	0.34		
PF04	**5**	0.64	0.70	0.66
PF05	**6**	n/a		

Table 6

Results for the OPAL framework using the AIC and BIC weights for model selection.

Model	Occam category	AIC *w*	BIC*w*	$D_{\mathrm{KL}}(\sigma^2_{16})$	$D_{\mathrm{KL}}(\sigma^2_{18})$
RD01	**1**	n/a	n/a	0.92	0.70
PF01	**2**	n/a	n/a	0.65	0.74
RD02	**3**	0.41	0.41	0.95	0.72
RD03	**3**	0.25	0.25		
MD01	**3**	0.34	0.34		
RD04	**4**	0.02	0.02		
MD02	**4**	0.08	0.08		
MD03	**4**	0.05	0.05		
PF02	**4**	0.85	0.85	0.68	0.76
MD04	**5**	0.02	0.02		
PF03	**5**	0.52	0.52	0.64	0.70
PF04	**5**	0.46	0.46		
PF05	**6**	n/a	n/a		

Math Models Methods Appl Sci. Author manuscript; available in PMC 2017 November 01.